Research Article
Vol. 8, No. 6 | 1 Jun 2017 | BIOMEDICAL OPTICS EXPRESS 2965
Biomedical Optics EXPRESS

Photothermal imaging of skeletal muscle mitochondria

TORU TOMIMATSU,[1] JUN MIYAZAKI,[1] YUTAKA KANO,[2] AND TAKAYOSHI KOBAYASHI[1,2,3,*]

[1] *Advanced Ultrafast Laser Research Center, The University of Electro-Communications, 1-5-1 Chofugaoka, Chofu, Tokyo 182-8585, Japan*
[2] *Brain Science Inspired Life Support Research Center, The University of Electro-Communications, 1-5-1 Chofugaoka, Chofu, Tokyo 182-8585, Japan*
[3] *Advanced Ultrafast Laser Research Center, Department of Electrophysics, National Chiao-Tung University, 1001 Ta Hsinchu Rd., Hsinchu 300, Taiwan*
[*] *kobayashi@ils.uec.ac.jp*

Abstract: The morphology and topology of mitochondria provide useful information about the physiological function of skeletal muscle. Previous studies of skeletal muscle mitochondria are based on observation with transmission, scanning electron microscopy or fluorescence microscopy. In contrast, photothermal (PT) microscopy has advantages over the above commonly used microscopic techniques because of no requirement for complex sample preparation by fixation or fluorescent-dye staining. Here, we employed the PT technique using a simple diode laser to visualize skeletal muscle mitochondria in unstained and stained tissues. The fine mitochondrial network structures in muscle fibers could be imaged with the PT imaging system, even in unstained tissues. PT imaging of tissues stained with toluidine blue revealed the structures of subsarcolemmal (SS) and intermyofibrillar (IMF) mitochondria and the swelling behavior of mitochondria in damaged muscle fibers with sufficient image quality. PT image analyses based on fast Fourier transform (FFT) and Grey-level co-occurrence matrix (GLCM) were performed to derive the characteristic size of mitochondria and to discriminate the image patterns of normal and damaged fibers.

OCIS codes: (170.0170) Medical optics and biotechnology; (170.0110) Imaging systems; (350.5340) Photothermal effects.

References and links

1. L. E. Bakeeva, Chentsov YuS, and V. P. Skulachev, "Mitochondrial framework (reticulum mitochondriale) in rat diaphragm muscle," Biochim. Biophys. Acta **501**(3), 349–369 (1978).
2. M. Picard, K. White, and D. M. Turnbull, "Mitochondrial morphology, topology, and membrane interactions in skeletal muscle: a quantitative three-dimensional electron microscopy study," J. Appl. Physiol. **114**(2), 161–171 (2013).
3. M. Picard, B. J. Gentil, M. J. McManus, K. White, K. St Louis, S. E. Gartside, D. C. Wallace, and D. M. Turnbull, "Acute exercise remodels mitochondrial membrane interactions in mouse skeletal muscle," J. Appl. Physiol. **115**(10), 1562–1571 (2013).
4. B. Glancy, L. M. Hartnell, D. Malide, Z. X. Yu, C. A. Combs, P. S. Connelly, S. Subramaniam, and R. S. Balaban, "Mitochondrial reticulum for cellular energy distribution in muscle," Nature **523**(7562), 617–620 (2015).
5. J. B. Gale, "Mitochondrial swelling associated with exercise and method of fixation," Med. Sci. Sports **6**(3), 182–187 (1974).
6. P. D. Gollnick and D. W. King, "The immediate and chronic effect of exercise on the number and structure of skeletal muscle mitochondria," Biochem. Exerc. Med. Sport **3**, 239–244 (1969).
7. D. E. Kelley, J. He, E. V. Menshikova, and V. B. Ritov, "Dysfunction of mitochondria in human skeletal muscle in type 2 diabetes," Diabetes **51**(10), 2944–2950 (2002).
8. M. W. Hulver, J. R. Berggren, R. N. Cortright, R. W. Dudek, R. P. Thompson, W. J. Pories, K. G. MacDonald, G. W. Cline, G. I. Shulman, G. L. Dohm, and J. A. Houmard, "Skeletal muscle lipid metabolism with obesity," Am. J. Physiol. Endocrinol. Metab. **284**(4), E741–E747 (2003).
9. C. T. Moraes, E. Ricci, E. Bonilla, S. DiMauro, and E. A. Schon, "The mitochondrial tRNA($^{\mathrm{Leu(UUR)}}$) mutation in mitochondrial encephalomyopathy, lactic acidosis, and strokelike episodes (MELAS): genetic, biochemical, and morphological correlations in skeletal muscle," Am. J. Hum. Genet. **50**(5), 934–949 (1992).

#284859
https://doi.org/10.1364/BOE.8.002965
Journal © 2017
Received 18 Jan 2017; revised 1 May 2017; accepted 2 May 2017; published 15 May 2017

10. T. Shimada, K. Horita, M. Murakami, and R. Ogura, "Morphological studies of different mitochondrial populations in monkey myocardial cells," Cell Tissue Res. **238**(3), 577–582 (1984).
11. T. Ogata and Y. Yamasaki, "Ultra-high-resolution scanning electron microscopy of mitochondria and sarcoplasmic reticulum arrangement in human red, white, and intermediate muscle fibers," Anat. Rec. **248**(2), 214–223 (1997).
12. A. V. Kuznetsov, Y. Usson, X. Leverve, and R. Margreiter, "Subcellular heterogeneity of mitochondrial function and dysfunction: evidence obtained by confocal imaging," Mol. Cell. Biochem. **256**(1-2), 359–365 (2004).
13. F. Shi, H. He, Y. Wang, D. Liu, M. Hu, and C. Wang, "Mitochondrial swelling and restorable fragmentation stimulated by femtosecond laser," Biomed. Opt. Express **6**(11), 4539–4545 (2015).
14. I. I. Pipinos, S. A. Swanson, Z. Zhu, A. A. Nella, D. J. Weiss, T. L. Gutti, R. D. McComb, B. T. Baxter, T. G. Lynch, and G. P. Casale, "Chronically ischemic mouse skeletal muscle exhibits myopathy in association with mitochondrial dysfunction and oxidative damage," Am. J. Physiol. Regul. Integr. Comp. Physiol. **295**(1), R290–R296 (2008).
15. P. L. Gourley, J. K. Hendricks, A. E. McDonald, R. G. Copeland, K. E. Barrett, C. R. Gourley, K. K. Singh, and R. K. Naviaux, "Mitochondrial correlation microscopy and nanolaser spectroscopy - new tools for biophotonic detection of cancer in single cells," Technol. Cancer Res. Treat. **4**(6), 585–592 (2005).
16. A. V. Brusnichkin, D. A. Nedosekin, E. I. Galanzha, Y. A. Vladimirov, E. F. Shevtsova, M. A. Proskurnin, and V. P. Zharov, "Ultrasensitive label-free photothermal imaging, spectral identification, and quantification of cytochrome *c* in mitochondria, live cells, and solutions," J. Biophotonics **3**(12), 791–806 (2010).
17. D. A. Nedosekin, E. I. Galanzha, S. Ayyadevara, R. J. Shmookler Reis, and V. P. Zharov, "Photothermal confocal spectromicroscopy of multiple cellular chromophores and fluorophores," Biophys. J. **102**(3), 672–681 (2012).
18. J. Miyazaki, H. Tsurui, K. Kawasumi, and T. Kobayashi, "Optimal detection angle in sub-diffraction resolution photothermal microscopy: application for high sensitivity imaging of biological tissues," Opt. Express **22**(16), 18833–18842 (2014).
19. J. Miyazaki, H. Tsurui, and T. Kobayashi, "Reduction of distortion in photothermal microscopy and its application to the high-resolution three-dimensional imaging of nonfluorescent tissues," Biomed. Opt. Express **6**(9), 3217–3224 (2015).
20. J. Miyazaki, H. Tsurui, K. Kawasumi, and T. Kobayashi, "Simultaneous dual-wavelength imaging of nonfluorescent tissues with 3D subdiffraction photothermal microscopy," Opt. Express **23**(3), 3647–3656 (2015).
21. D. Lasne, G. A. Blab, F. De Giorgi, F. Ichas, B. Lounis, and L. Cognet, "Label-free optical imaging of mitochondria in live cells," Opt. Express **15**(21), 14184–14193 (2007).
22. J. He, J. Miyazaki, N. Wang, H. Tsurui, and T. Kobayashi, "Biological imaging with nonlinear photothermal microscopy using a compact supercontinuum fiber laser source," Opt. Express **23**(8), 9762–9771 (2015).
23. Y. Kano, K. Sampei, and H. Matsudo, "Time course of capillary structure changes in rat skeletal muscle following strenuous eccentric exercise," Acta Physiol. Scand. **180**(3), 291–299 (2004).
24. J. Adur, L. D. Souza-Li, M. V. Pedroni, C. E. Steiner, V. B. Pelegati, A. A. D. Thomaz, H. F. Carvalho, and C. L. Cesar, "The severity of osteogenesis imperfecta and type I collagen pattern in human sukin as determined by nonlinear microscopy: Proof of principle of a diagnostic method," PLoS One **8**(7), e69186 (2013).
25. A. Materka, "Texture analysis methodologies for magnetic resonance imaging," Dialogues Clin. Neurosci. **6**(2), 243–250 (2004).

---

1. Introduction

Energy delivery activities in skeletal muscle are mediated by circumstantial morphological changes in the mitochondria [1–4]. The morphology of the mitochondria is of vital importance for the physiological functions of muscle, particularly in relation to exercise [3, 5, 6] or to disease states, such as diabetes [7], obesity [8], and mitochondrial encephalomyopathies [9]. Skeletal muscle fibers normally possess two mitochondrial populations that differ in subcellular location: subsarcolemmal (SS) mitochondria accumulate underneath the sarcolemma, and intermyofibrillar (IMF) mitochondria are located between the myofibrils in the fiber center, forming an ordered pattern [2, 3]. Mitochondria further undergo fusion to form the reticulum and divide into discrete organelles during dynamic activities. Because mitochondria show a variety of shapes in skeletal muscle, easily applied imaging techniques are desired for a large number of observations for studies of mitochondrial functions.

Transmission electron microscopy (TEM) is the most powerful tool for accurate morphological analysis and has a spatial resolution of nanometer scale [1–3,10]. Scanning electron microscopy (SEM), with sample preparation using OsO_4-based buffer [11] or SEM combined with a focused ion beam [4], allows visualization of the three-dimensional (3D) properties of mitochondria. These electron microscopic techniques, however, involve inevitably time-consuming sample preparation with several steps and are not suitable for routine application or for comparative study of many samples.

Other widely used methods are based on fluorescence microscopy, which allows observation following fluorescence labeling due to high chemical selectivity. Fluorescence microscopy has offered various approaches to assessing mitochondrial structures [12, 13] and contributed to diagnosis of myopathies [14] and cancer cells [15]. Labeling, however, can distort mitochondrial behavior via interactions between the label indicator and mitochondrion and also is subject to photo-bleaching, which restricts observations for a long duration.

A promising alternative to the above microscopic methodologies is photothermal (PT) microscopy, which allows nonfluorescent imaging via a phothothermal effect. The scheme of this method consists of photoexcitation of target having absorptivity at the pump wavelength and detection of the resulting change in the refractive index with a probe beam. The method is useful for imaging mitochondria by exploiting strong absorption at the possible absorbent molecule, cytochrome c [16, 17]. Thus, it does not involve the distortion of mitochondria due to the labeling process. In addition, its advantages include simplification of sample preparation due to the absence of a requirement for labeling and its superior resolution (lateral, ~200 nm; depth, ~500 nm) achieved by the quadratic dependence of the point spread function in pump-probe configuration [18–20]. To date, PT imaging of mitochondria has been performed only in limited tissue types, including nematodes [17], HeLa cells [16, 21], and kidney cells [21, 22]. The application of PT microscopy to skeletal muscle mitochondria has not been reported despite the importance of the morphological characteristics of these mitochondria. For the imaging of skeletal muscle mitochondria, the image analysis also plays substantial role in assessing the various structures of mitochondria, because its morphologies are associated with the energy delivery activities in the muscle. The quantitative evaluation of such mitochondrial transition is essential for future application to the diagnosis of mitochondria.

In this study, we propose the sequential process combining PT imaging technique and its image analysis methodologies for skeletal muscle mitochondria. We demonstrate PT imaging in unstained and stained muscle tissues using PT microscopy in which an auto-balanced detector with laser diodes was incorporated [18–20]. The mitochondrial network structures were successfully imaged with sufficient image quality by our highly sensitive PT imaging system. We applied this method to muscle fibers after exercise to compare the 2D PT images of normal and damaged muscle fibers and qualitatively evaluated the morphological changes in the mitochondria by fast Fourier transform (FFT) and grey level co-occurrence matrix (GLCM) analyses.

2. Sample preparation

To observe the microstructures in muscle fibers by both bright field images and PT images, the fixed sections of the muscle fibers were used. The gastrocnemius muscles of anaesthetized male Wistar rats (Japan SLC, Shizuoka) were subjected to 300 controlled eccentric contractions using electrical stimulation (100 Hz, 700 ms, ~10 V, one contraction every 3 s). One day after eccentric exercise, tissues fixation was performed by *in situ* perfusion [23] for the conservation of internal microstructure of fibers in living state. After fixation, gastrocnemius muscles were carefully dissected, and the mid-belly region was cut transverse to the long axis of the muscle and trimmed into blocks (approximately 2 × 2 × 1 mm^3 in size). The block was post-fixed in 1% osmium tetroxide for 2–3 h, dehydrated through a series of increasing concentrations of ethanol, cleared in propylene oxide, and embedded in Epon 812 (Quetol 812, Nishin-EM, Tokyo). The 1-μm thick sections were prepared by cutting a block that was transverse to the muscle fiber axis in a microtome. Mitochondrial imaging was performed using unstained tissue and tissue stained with a 1% aqueous solution of toluidine blue.

3. Experimental setup

The setup of the PT imaging system is shown in Fig. 1. Lasers with wavelengths of 488 nm and 638 nm were used as the PT pump and the probe beam, respectively. The output from the pump laser was intensity-modulated to 100 kHz with a signal generator (Rigol, DG4162) for lock-in detection. Both pump and probe beams were introduced into single-mode fibers and to doublet lenses with a focal length of 50 mm for the formation of Gaussian intensity profiles with a lateral width of ~10 mm. The two laser beams were then coupled to a dichroic mirror and illuminated on the sample through the objective lens (magnification, 40 × ; numerical aperture, 0.95). The modulated intensity of probe signal generated by the PT effect on the sample induced by pumping was collected with the condenser lens and detected with an auto-balanced detector (Newfocus, Nirvana). To avoid image distortion due to twin peak generation in PT signal [19], the focal position of the pump beam was set ~0.5 μm forward of that of the probe beam. The pump beam that passed through the sample was removed with a band-pass filter. The probe intensity signal was finally introduced to a lock-in amplifier (Signal Recovery, Model 7270DSP). The probe intensity modulation was recorded as a function of the illuminated sample position by moving the closed-loop x-y-z piezo stage with a positioning resolution of 5 nm to create the PT image.

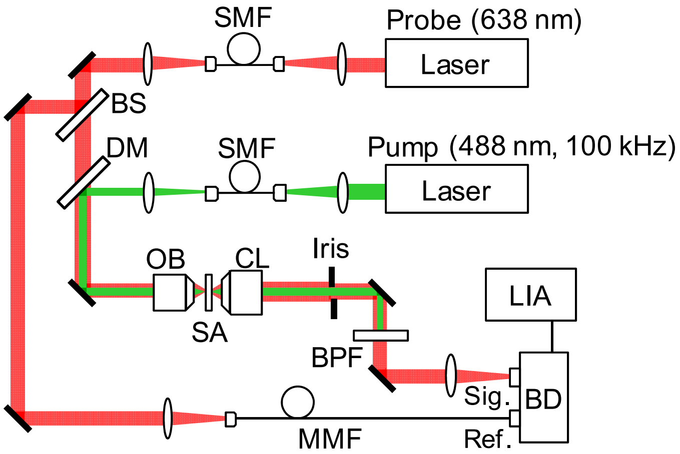

Fig. 1. Schematics of PT microscopy. BS: beam splitter, DM: dichroic mirror, OB: objective lens, CL: condenser lens, SA: sample, BPF: band pass filter, SMF: single mode fiber, MMF: multimode fiber, BD: auto-balanced detector, LIA: lock-in amplifier.

4. Results

A PT image of unstained muscle tissue was first studied in comparison with that of stained tissue. Figure 2(a) and 2(b) show bright field images of identical areas of tissue sections without and with toluidine-blue staining, taken from the same body several micrometers apart in depth. In bright field images, no noticeable differences in cell geometry between the two sections were found despite differences in the sectioning depth. For both sets of tissues, PT images were acquired for a 20 × 20 μm^2 area with a total of 200 × 200 pixels with a pixel dwell time of 2 ms, corresponding to a frame acquisition time of ~80 s. The powers of the pump for the excitation were set to 1.0 mW and 0.1 mW for unstained and stained tissues, respectively, and the power of the probe was set to 1.0 mW for both sets of tissues. Figure 2(c) and 2(d) show PT images of the same rectangular area in Fig. 2(a) and 2(b), respectively. We observed a branched network structure, even in unstained tissue (Fig. 2(c)), and this network pattern was highlighted clearly in the stained tissue with a characteristic size of ~1 μm (Fig. 2(d)), whereas the network pattern was smeared in bright field images for both tissues. This structure is attributed to the reticulum of IMF mitochondria due to its similarity to the mitochondrial profiles reported in earlier TEM and SEM studies [1–4] with respect to their geometry and size scale. By carefully comparing the noise-reduced images obtained by line filters in the fast Fourier transform (FFT) analysis, as shown in Fig. 2(e) and 2(f), the network geometries in the two sections were found to be quite similar. This finding is consistent with the fact that the mitochondrial network transpierces the entire body of the cell [1, 4, 11]. The rough matching of the PT patterns between two sections also implies that PT signals for the stained tissue by toluidine blue mainly originate from the mitochondria as well as for the unstained tissue and the staining doesn't provoke large distortion of mitochondrial structures.

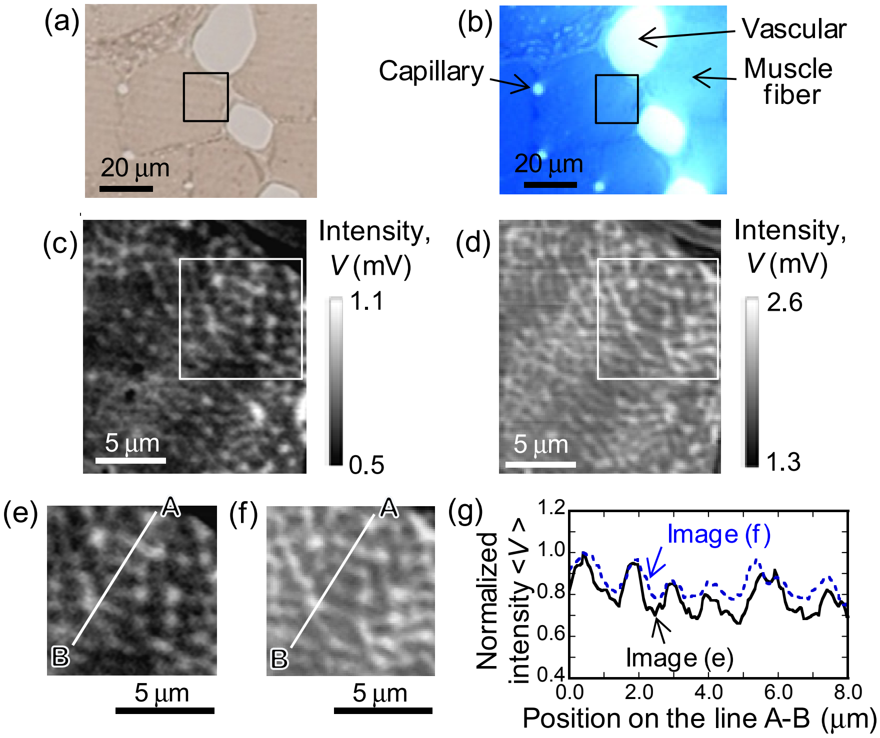

Fig. 2. (a, b) Bright field images in identical structure area for skeletal muscle tissues without and with toluidine blue staining. (c, d) PT images on the area outlined by black rectangles on (a, b). (e, f) PT images at white square area on (c, d), where the lateral line noise arising from the instability of stage motion is reduced by the line filter of FFT. (g) Normalized intensity profiles on line A-B in (e) and (f). Pump laser powers are 1.0 mW and 0.1 mW for measurement of unstained and stained tissue, respectively. Probe laser powers are 1 mW for both tissues.

The image quality of the network structure in unstained tissue (signal-to-noise ratio (SNR) of 25) was relatively lower than that for stained tissue (SNR of 53). Because the PT effect seems to originate from cytochrome c in mitochondria in unstained tissue [16, 17], whereas toluidine blue is the main target in stained tissue, differences in the image quality of the two PT images can be interpreted by differences in absorbance between the targets. Indeed, the absorption difference emerges in PT signal magnitude. The signal intensity in unstained tissue was about half that in stained tissue despite about 10 times greater pump power for unstained tissues than for stained tissues, as shown in Fig. 2(c) and 2(d). In contrast, the PT image contrast for stained tissue was weaker than that for unstained tissue, as evident from the signal line profiles shown in Fig. 2(g). Although the cytochrome c is concentrated in the mitochondria, toluidine blue is bound to various proteins even outside of the mitochondria, resulting in poor image contrast in stained tissues due to spread distribution of the toluidine blue density.

Our findings demonstrate that mitochondrial structures can be clearly resolved in PT images with higher contrast than in bright field images. Image quality of mitochondria in present system is equal to or greater than that of previous PT methods [16, 17, 21, 22], which allows us to visualize even smaller structure of mitochondria, as described below. The results also indicate that present method can be appreciable even for tissues of probably lower concentration of cytochrome c caused by the tissue fixation. We also confirmed our technique was available for raw skeletal muscle samples without staining; bare muscle pieces peeled from thigh of a live rat, where fine mitochondria reticulum was still clearly visible despite the thick (~500 μm) sample (not shown).

To examine the mitochondrial structure in more detail, we focused on PT imaging of fixed sections of the stained tissue. Figure 3 shows bright field images and PT images for muscle fibers 1 day after exercise. From the bright field images, normal muscle fibers with an average size of approximately 40 μm and abnormally swollen round fibers were present (Fig. 3(a) and 3(c), respectively). The swollen fibers were present in approximately 77% of the muscle fibers, which is comparable with findings of earlier works [23].

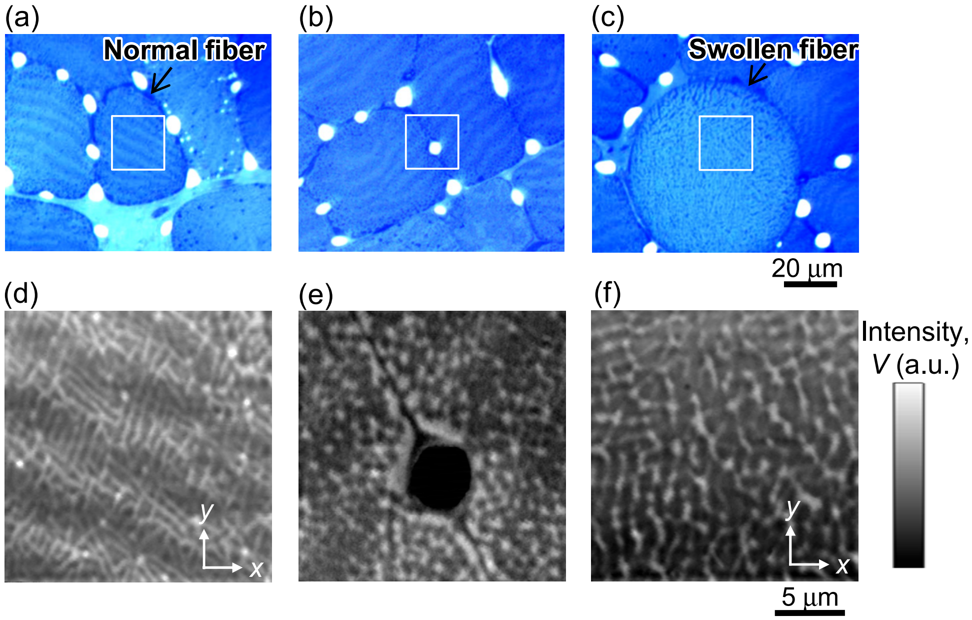

Fig. 3. Images of stained tissues of muscle fibers for 1 day after excising. (a-c) Bright field images of three different areas. (d-f) PT images taken on the square area on (a-c), corresponding to the area at the center of the normal fiber (d), near the capillary (e), and at the center of the swollen fiber (f). Pump and probe laser powers are 50 μW and 1 mW, respectively.

In normal fibers, the PT images showed two types of structures: the IMF network inside the fiber (Fig. 3(d)) and locally aggregated structures near the capillary (Fig. 3(e)), which correspond well to the features of SS mitochondria [2,3]. As seen in Fig. 3(d), our PT system has a capability to clearly visualize the small mitochondria with a size of ~300 nm at minimum. In the IMF mitochondrial structure, stripe contrast with a periodicity of 4 to 6 μm was discernible. This long-scale stripe was also identified in bright field images as a contrast (Fig. 3(a)) with the same periodicity as in the PT image (Fig. 2(a)). This stripe is caused by periodic mitochondrial density fluctuations appearing in a slightly inclined section toward the plane of the z-disc structure of myofibrils [1, 2] and the deeply stained region corresponds to a zone of higher mitochondrial density. The stripes in the PT signal were also present in the unstained and stained tissues shown in Fig. 2(c) and 2(d), respectively. The stripe positions in the two tissues were slightly shifted. This stripe shift was caused by sectioning at the different depth positions of well-ordered and slightly tilted mitochondria structures.

In contrast to the stripe structure found in the normal fibers, this pattern was not found in the swollen muscle fibers in either the bright field (Fig. 3(c)) or PT (Fig. 3(f)) images, probably because of the disruption in the ordered structure of the myofibrils. Consequently, the fine network structure observed in normal fibers was no longer present in swollen fibers.

We performed the FFT analysis of the PT images to assess the characteristic size of mitochondrial distribution in both normal and swollen fibers. Here, PT images of the stained tissue with high SNR signal was employed to explore the optimum methodology of PT image analyses. The signal intensity profiles of 36 lines were extracted randomly in a certain angle of PT images, which were applied to the analysis of 12 angles with 15-degree angle steps for 432-line acquisition. Figure 4(a) and 4(b) show the average power spectra of the images of normal and swollen fibers for the images in Fig. 3(a) and 3(c), respectively. The power spectra of normal fibers (Fig. 4(a)) consisted of two peaks; a sharp peak on the low wave number side, corresponding to a mitochondria density stripe, and a broad peak on the higher wave number side, corresponding to the mitochondrial reticulum. In contrast, one broad peak was observed in the spectra for swollen fibers (Fig. 4(b)). In addition, the power spectra showed angular dependence for both types of fibers.

To address the morphology of the mitochondrial structure, mean spatial frequencies, μ, and standard deviations, σ, of power spectra were evaluated by deriving the first and second moments of the power spectra as follows:

$$\mu = \frac{\int_{k_1}^{k_2} A \cdot k dk}{\int_{k_1}^{k_2} A dk}, \tag{1}$$

$$\sigma = \left[\frac{\int_{k_1}^{k_2} A \cdot (k-\mu)^2 dk}{\int_{k_1}^{k_2} A dk} \right]^{0.5}, \tag{2}$$

where A is the amplitude of the power spectra, and k is the wave number. k_1 and k_2 were determined as k_1^{-1} = 0 µm, and k_2^{-1} = 2 µm, respectively, so that signals with an amplitude comparable to the noise level were removed to reduce the white noise-induced variation in μ and σ. For the normal fibers, before calculation of the two values, the background caused by the mitochondrial stripe was subtracted by fitting a Gaussian profile to the peak of the lower wave number lying in the range, $k < 0.35$ µm^{-1}. The maximum value of μ over all profile angles, which is $\mu_{\max}$, for four normal and four swollen fibers are plotted with σ of the corresponding spectrum, $\sigma_{\max}$ in Fig. 4(c). $\mu_{\max}$ values for swollen fibers were in all the cases smaller than those for normal fibers by a deviation of more than 0.05 µm^{-1}, whereas $\sigma_{\max}$ for both fiber types showed similar values, even after subtracting the low frequency peak component of the mitochondrial stripe from the normal fibers. The reduction in $\mu_{\max}$ with a constant $\sigma_{\max}$ in swollen fibers demonstrated the increased mitochondrial size and the disappearance of the high-frequency component of the mitochondria network ($k \sim 1$ µm^{-1}). The characteristic mitochondrial sizes derived by the inverse of average $\mu_{\max}$ were ~1.2 µm and ~1.5 µm for normal and swollen fibers, respectively, as shown in the Table in Fig. 4(c).

This change is consistent with the feature of well known mitochondrial swelling reported for exhaustively exercised muscle [5, 6].

Furthermore, we found larger standard deviations in mitochondrial sizes among swollen fibers (0.11 μm) than those among normal fibers (0.06 μm), which was due to the large variety of changes in mitochondrial morphology during the damage process that was also manifested as larger spectral peak width for swollen fibers (1.63 μm) than for normal fibers (1.04 μm) (Table in Fig. 4(c)).

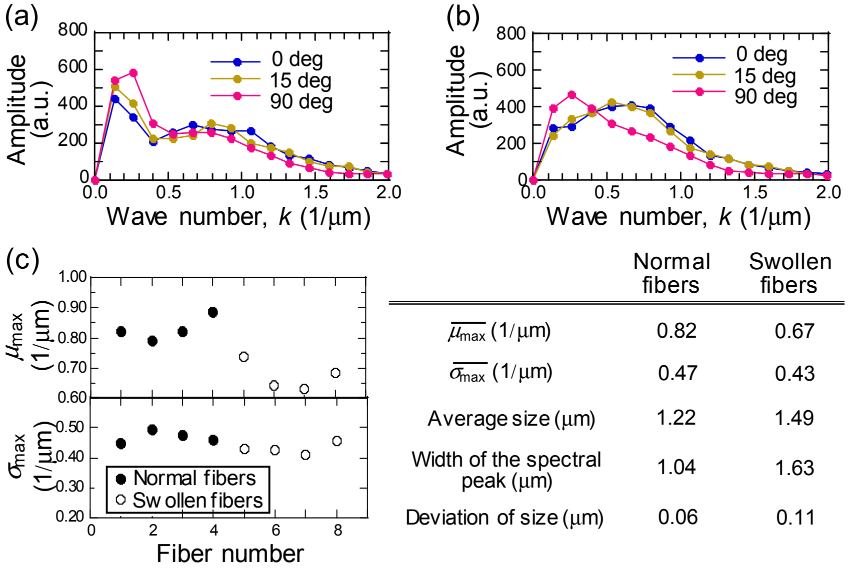

	Normal fibers	Swollen fibers
$\overline{\mu_{\max}}$ (1/μm)	0.82	0.67
$\overline{\sigma_{\max}}$ (1/μm)	0.47	0.43
Average size (μm)	1.22	1.49
Width of the spectral peak (μm)	1.04	1.63
Deviation of size (μm)	0.06	0.11

Fig. 4. 1D-FFT power spectra of PT image profiles for the normal fiber and the swollen fiber for images of Fig. 3(d) and 3(f), respectively. Line profile at 0, 15, and 90 degree from x axis defined in Fig. 3 are plotted. Power spectra are calculated by averaging spectra for 36 signal profiles for each angles with a sampling length of 7.5 μm. (c) Largest mean wave number of power spectra over all profile angles, $\mu_{\max}$, and corresponding standard deviation, $\sigma_{\max}$. $\overline{\mu_{\max}}$ and $\overline{\sigma_{\max}}$ in the Table are calculated by averaging $\mu_{\max}$ and $\sigma_{\max}$ over four normal and four swollen fibers, respectively. Average size, width of the spectral peak, and deviation of size in the Table are derived from inverse of $\overline{\mu_{\max}}$, $\overline{\sigma_{\max}}$ and the deviation of $\overline{\mu_{\max}}$ among fibers, respectively.

The geometrical arrangement of mitochondria with high-order characteristics including more complex structural properties was further evaluated. This was performed by the statistical texture analysis based on the gray level co-occurrence matrix (GLCM) composed of occurrence probabilities of pairs of pixel grey levels in an image [24, 25]. As a parameter of importance to periodical patterns, we focused on the image correlation, an indication of a linearity of grey level relations between two pixels for the specific distance and orientation and a periodic feature yields higher linearity of grey level pairs, i.e., higher correlations, at their wavelength. GLCM correlation, C, was given by,

$$C = \sum_i \sum_j \frac{(i - m_i)(j - m_j)}{s_i \cdot s_j} P(i, j), \tag{3}$$

where $P(i,j)$ is a normalized $(i,j)^{\text{th}}$ element of co-occurrence matrix, m_i is an expected value, $m_i = \sum_i i \sum_j P(i,j)$, and s is a standard deviation, $s_i = \sqrt{\sum_i (i-m_i)^2 \sum_j P(i,j)}$, over all matrix elements [24]. The analyzing area of images were set to 7 × 7 μm^2. Figure 5(a) and 5(b) are the C values versus distance between two pixels, d, for the normal and the swollen fiber computed from the images of Fig. 3(d) and 3(f) with the orientation, θ = 45 degree from x axis on Fig. 3. The parameter C rapidly decreased with distance between two pixels, d, in the vicinity of the d = 0 μm for the normal fiber (Fig. 5(a)). From d = 0.6 μm, however, the slope of the C decrease became smaller and C started to be oscillatory. The oscillation of the C profile corresponds to a periodically distributed mitochondrial structure in the image, as described above. The peak positions of the C oscillation profiles, d_{peak}, for different θ are plotted in Fig. 5(c) and 5(d). For the normal fiber (Fig. 5 (c)), we found the periodical emergence of d_{peak} at positions of integer multiples of fundamental wavelengths along d direction, persisting up to d = 4.5 μm. It was also found that d_{peak} exhibited arch dependence on θ, which arose from straight-lines based texture lying on PT images of the normal fiber. Indeed, the θ dependence of d_{peak} were well fitted by blue curves shown in Fig. 5(c) derived by the spacing of a straight line fringe assumed on the real x-y space,

$$d_{\text{peak}} = \Delta d_{\text{f}} / \cos(\theta - \theta_{\text{f}}), \tag{4}$$

where Δd_{f} and θ_{f} are the spacing and the orientation of a straight line fringe. The d_{peak} map of Fig. 5(c) explicitly extracted the dominant two fringes lying on θ = 0-110 and 110-180 degree that constituted the mitochondrial reticulum in the normal fiber. The swollen fiber, on the other hand, induced the disappearance of such the arch dependence on θ in addition to the weakened periodicity of d_{peak} along d direction (Fig. 5(d)). These analysis results show superior discrimination capability of the texture of normal and swollen fibers by extracting the periodicity of correlations of the PT image patterns.

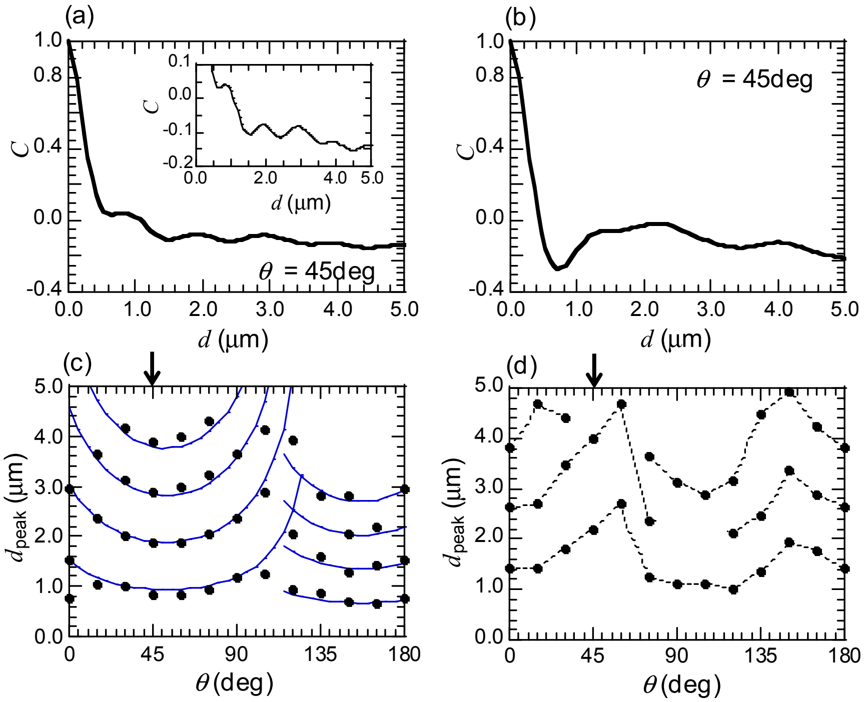

Fig. 5. (a, b) The profiles of correlation, *C*, for the PT images for the normal fiber (shown in Fig. 3 (d)) and the swollen fiber (shown in Fig. 3(f)), respectively. *C* are calculated for two pixels separated with a distance, *d*, by GLCM analysis on the image size for 7 × 7 μm^2. The orientation angle of two pixels, θ, is $\theta = 45$ deg from the x axis depicted in Fig. 3, indicated in arrows in (c) and (d). Inset: Enlarged curve of *C* profile for the normal fiber. (c, d) The peak positions of the *C* profiles, d_{peak}, for different angle, θ, for the normal and the swollen fiber, respectively. The blue curves in (c) are the fitted profiles by equally spaced arch-shape curves, corresponding to equally spaced straight lines in x-y real space.

Comparison of the characteristic size and the anisotropy of patterns was made between normal and swollen fibers by the d_{peak} spacing, Δd, varying with θ. Δd were calculated by averaging the spacing of d_{peak} within a range of d = 0-2.0 μm for 12 orientations on each image texture. Hereafter, the minimum value of Δd, Δd_{min} was defined as the swelling index. Figure 6 shows Δd plots of the maximum value, Δd_{max}, versus the swelling index (Δd_{min}) for eight normal and eight swollen fibers. The swelling index could well discriminate between the mitochondria in normal fibers and in swollen fibers. From the plots, the critical size of swelling index, where the regular mitochondrial structure starts to collapse, was found to be Δd_{min} ~0.9 μm. This critical size was smaller than characteristic size derived from FFT analysis for both the normal (~1.2 μm) and the swollen (~1.5 μm) fiber. Due to high performance for analyzing local features [25], the GLCM correlations extracted a short range periodicity, whereas it was hidden by the background of lower wave number components in the case of FFT, resulting in the larger calculated values of characteristic sizes. The swelling index for normal fibers displayed the small standard deviation (~0.09 μm), reflecting the conservation of the regular structure composed of myofibril over the normal fibers. While, the swelling index showed larger deviation for swollen fibers (~0.22 μm) than for normal fibers and was also larger than that of FFT result (the standard deviation of μ_{max}^{-1} for swollen fibers: 0.11 μm). It was evident from this fact that the GLCM correlation sensitively discriminated spatial features for swollen mitochondria at different stage of fibers damaging. In contrast, the aspect ratios, r ($r = \Delta d_{\max}/\Delta d_{\min}$), for normal fibers showed larger dispersion (r = 1.5-3.5) compared to r dispersion for swollen fibers (r = 1.7-2.3), implying that normal fibers have wide variety of anisotropy than swollen one in the mitochondrial network structure. These results are not largely affected by the tissue staining effect, which is evident from the matching of PT image patterns for unstained and stained tissues, as shown in Fig. 2. These calculations are useful for understanding the structural scale order of mitochondrial distribution. In addition, these types of analyses exploiting PT imaging are particularly suited to an application requiring a large amount of observation data, because a shorter acquisition time can be achieved by optimizing instrumental conditions.

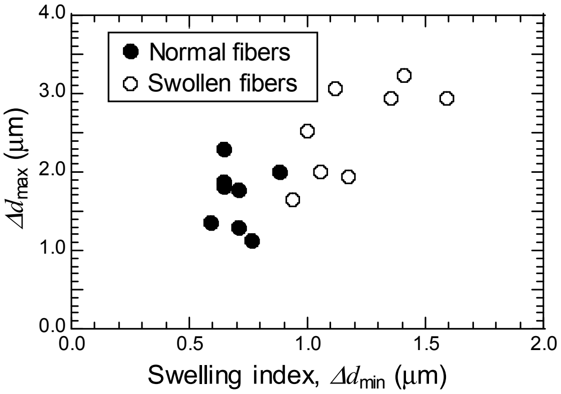

Fig. 6. Maximum d_{peak} spacing, $\Delta d_{\max}$, versus minimum d_{peak} spacing (swelling index), $\Delta d_{\min}$, of PT image patterns for normal and swollen fibers.

5. Conclusions

In previous PT techniques, a unique feature of skeletal muscle mitochondria, i.e., the changes in their shapes in response to metabolic demands or external stimulations, has not been studied, probably owing to poor image quality or time-consuming imaging process. In this work, we demonstrated mitochondrial imaging by simple and high sensitive PT technique and further apply its high quality images to systematic evaluation of mitochondrial morphology in the skeletal muscle. To the best of our knowledge, this is the first example of PT label-free imaging and identification of the structure of skeletal muscle mitochondria with the characteristic size of ~1 μm. The structures of IMF and SS mitochondria and the swelling of the mitochondria in muscle fibers were clearly resolved in PT images with higher contrast than in bright field images. The technically important aspect of our findings is that present method can be appreciable for tissues of probably lower concentration of cytochrome c caused by the tissue fixation. Simple FFT analysis of the mitochondria in normal and swollen fibers revealed changes in average size and its standard deviation of mitochondria caused by mitochondrial swelling in damaged fibers. The GLCM correlation explicitly reflected the periodic patterns of PT images. Its profiles confirmed changes in spacing, the angle dependence, and the aspect ratio of mitochondrial distribution, demonstrating that we could distinguish the mitochondrial structures of normal and damaged fibers and the method even offered a tool to qualitatively study the mitochondrial features at different fiber damage level. Although these image analyses were performed for stained tissues in this study, the application of proposed methods to label-free PT images are promising by further optimization and improvement of experimental system to increase the SNR of the PT signals. The simple method described here can be easily applied even to thicker samples, which will provide 3D morphological investigation of mitochondria with short acquisition time.